

Spin-flip scattering in magnetic tunnel junctions: From current-voltage characteristics to spin-transfer torque

J. Z. Sun ^{*}

IBM T. J. Watson Research Center, Yorktown Heights, New York 10598, USA



(Received 19 November 2020; revised 17 February 2021; accepted 17 March 2021; published 25 March 2021)

We examine room temperature current-voltage (IV) characteristics of CoFeB|MgO|CoFeB type of perpendicularly magnetized tunnel junctions developed for memory applications. From their nonlinear bias voltage dependence, a conductance “cross-scaling” is seen that is consistent with the involvement of inelastic spin-flip scattering in electrodes. A phenomenological model is constructed that connects the parameters of spin-flip scatter-related inelastic events with both magnetoresistance and spin-transfer torque. The model provides measurable, electrode-specific properties such as interface exchange stiffness as it affects spin-torque performance.

DOI: [10.1103/PhysRevB.103.094439](https://doi.org/10.1103/PhysRevB.103.094439)

I. INTRODUCTION

The room temperature conductance of a magnetic tunnel junction (MTJ) commonly increases with bias, due to mechanisms such as inelastic electron spin-flip scattering [1–7], inelastic electronic processes such as interface charge traps [8–11], as well as elastic processes involving band-structure-specific nonlinear conductance [12,13]. While many studies have been carried out to investigate the fundamental electronic-structures related bias dependence in MTJs, relatively little has been quantified for their room temperature properties that are important for memory applications.

The difficulty of understanding room temperature MTJ nonlinear behavior originates from the complexity of competing mechanisms present with similar magnitudes. This is the situation for both charge and spin-conductance analyses. It becomes therefore challenging to isolate a unique contributing factor in a given situation.

It however remains curious to notice that across MTJs of many types of tunnel barriers and ferromagnetic electrodes, a similar general behavior of conductance increase, and corresponding TMR reduction with bias is seen—for some examples, see Ref. [1,14–18] for non-MgO-based barriers, and Ref. [19–27] for MgO barrier based devices. It circumstantially suggests a common mechanism, perhaps large enough to be noticeable that is governing the leading order nonlinearity at room temperature. While band-structure related effects are present, the over-all behavior of ambient TMR versus bias appears quite robust against different types of barriers and electrodes.

Such ambient bias-dependent conductance is also seen in our CoFeB-MgO-based perpendicular tunnel junctions developed for memory applications. Our observations suggest a large portion of it is governed by tunnel electron’s spin-flip scattering [1,5,6,14]. Earlier we described the basic observation [28]. In this paper, we expand the discussion to connect the observation semiquantitatively to the effect of spin-flip

scattering process on spin-transfer torque (STT), thus relating the measured MTJ’s current-voltage (IV) characteristics to its STT bias dependence as they both are connected to bias-dependent spin-flip scatter rates.

II. ROOM TEMPERATURE BIAS DEPENDENCE OF A CoFeB-MgO-CoFeB TYPE OF MTJ

An example of the IV and related bias-dependent quantities are illustrated in Fig. 1. The junction shown here is about 80 nm in diameter, with CoFeB|MgO|CoFeB type of perpendicularly magnetized electrodes similar to what is described in Ref [29]. Figure 1(a) contains two IV branches corresponding to STT-induced magnetic switching between high- and low-conductance states. The red-colored branch labeled “P” is for measurement with up-sweeping V, in parallel state over the hysteresis region, and a parallel to antiparallel (P-to-AP) switch at the positive threshold voltage. The black branch labeled “AP” is the opposite branch with down-sweeping voltage, and a corresponding AP-to-P switch at a negative voltage threshold. This IV shown was 100 trace-averaged on triangular voltage bias sweeps at a frequency around 0.2 Hz.

Figure 1(b) gives the corresponding differential conductance. The zero-bias conductance corresponding to P and AP states are designated g_{p0} and g_{ap0} , respectively. An empirical transformation is made as

$$\Gamma_{p,ap}(V) = \frac{g_{p,ap}(V) - g_{p0,ap0}}{g_{ap0,p0}}, \quad (1)$$

which translates the curves in Fig. 1(b) into that of Fig. 1(c). Equation (1) “cross-normalizes” the P-branch’s conductance by the AP-branch’s zero-bias conductance, and vice versa. We note that the $\Gamma_{p,ap}(V)$ ’s voltage dependence slope in Fig. 1(c) has a dominant linear term, and that they show similar slope values (mostly within 2X) for both polarities.

The second-order derivative of the IVs are shown in Fig. 1(d). These are commonly used in tunnel spectroscopy for detecting additional scattering channels at elevated bias [30]. For our room temperature MTJ IVs, the blue dashed lines in Fig. 1(c) then corresponds to the respective blue

*jonsun@us.ibm.com

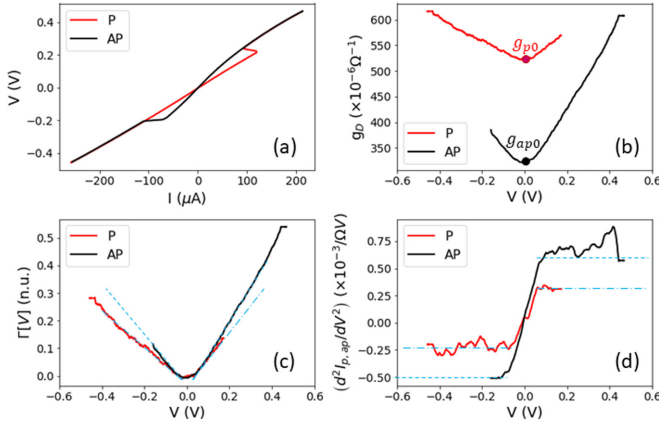


FIG. 1. IV characteristics related quantities of an MTJ. Room temperature measurement. (a) The IV curve of a device. (b) The differential conductance from (a), $g_D = dI/dV$. The zero-bias values are taken for g_{D0} and g_{ap0} for P and AP branches. (c) The “cross-normalized” conductance vs bias voltage, as defined by Eq. (1). Data beyond the STT-switching thresholds are truncated. The dashed blue lines illustrate the approximate linear voltage dependence, discussed later in Sec. 2. (d) The second-order differential conductance d^2I/dV^2 . The blue dashed lines illustrate the (nearly constant) average slopes of the spectral intensity related to the slopes in (c).

dashed level-lines in Fig. 1(d). The rounding near the $V = 0$ origin is related to thermal smearing of low-energy electronic states, with a reference energy scale as the ambient temperature $k_B T \sim 26$ mV. It may also in part be due to the presence of thermal magnons at ambient temperature. The slope in Fig. 1(c) is otherwise rather free of strong features, also evident from tunnel spectroscopy related second-order derivatives shown in Fig. 1(d).

These features presented in Fig. 1 could not be directly accounted for by zero-temperature band-structure related bias dependence. For an in depth discussion, a closer examination of our ambient IV curve with those from *ab initio* calculations is shown in the Supplemental Material [31].

Importantly, features shown in Fig. 1 appear across many types of different MTJ electrodes, and thus likely contain a common bias-dependence mechanism. In what follows, we present an empirical model demonstrating this common mechanism as likely originating from spin-flip scattering related magnetic excitation.

III. SPIN-SEPARATED CONDUCTANCE CHANNELS IN AN MTJ

A. Review of a simplified elastic spin-dependent tunnel model

To start, we revisit a spin-dependent magnetic tunnel junction model first introduced by John Slonczewski [32,33]. Following the assumptions in Refs. [1,10,33,34], we write the spin subband differential charge conductance of *elastic channels* between the reference (R) and free (F) electrodes separated by a tunnel barrier as

$$g_{\sigma,\sigma'}(V) = \frac{dJ_{\sigma,\sigma'}}{dV} = G_{\sigma,\sigma'}(V) \langle \sigma | \sigma' \rangle^2, \quad (2)$$

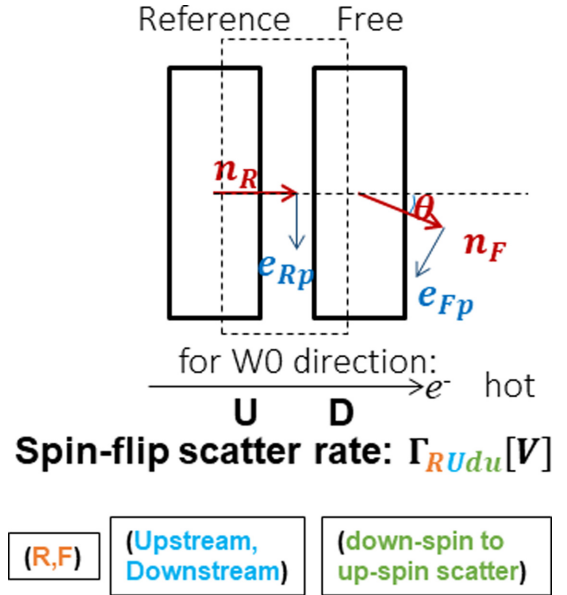


FIG. 2. An illustration of the tunnel junction under consideration, and definition of relevant symbols. An electrode-specific quantity, such as the spin-flip scatter rate Γ , is labeled by the electrode name “R” or “F” for reference or free as the first subscript, followed by the electrode’s relative positions (“U”, “D” for upstream or downstream), followed by the spin-flip direction from the subband indices (“du” for a minority band electron scattering into the majority band, and so on.)

where $\sigma(R)$ and $\sigma'(F) = |\pm\rangle = |_{\uparrow}^{\uparrow}\rangle$ are spin indices for R and F tunnel electrodes subband tunnel states, respectively. A rotation between F and R moments of angle θ gives $\langle |_{\uparrow}^{\uparrow}\rangle = \cos(\theta/2)$, and $\langle |_{\downarrow}^{\downarrow}\rangle = \pm \sin(\theta/2)$. $\theta = 0$ is the P state; $\theta = \pi$, the AP state. $G_{\sigma,\sigma'}$ are the spin-channel specific electron conductance. The geometry and indices are defined in Fig. 2.

We assume an R and F electrode “separability” [33] so that $G_{\sigma,\sigma'} = f \Omega_{R\sigma} \Omega_{F\sigma'}$, where the Ω s are the electrode’s interface spin-subband average density of states in their own spin-quantization direction, and summed over states involved [32,33,35]. The factor f represents the band-structure related quantity in the tunnel state summation [1,33]. For simplicity, we set $f = 1$ and let it be absorbed into the Ω s without loss of generality for our parametrization. We also use the low-bias limit assumption so that $\Omega_{R\sigma} \Omega_{F\sigma'}$ is taken as voltage-independent [33], which appears to be a reasonable assumption for CoFe alloyed electrodes except when approaching the very cobalt-rich limit and at biases well above 0.5 V. A more detailed discussion on this is given in the Supplemental Material [31] for a side-by-side comparison with *ab initio* results from Ref. [13].

¹Here, we use $|_{\uparrow}^{\uparrow}\rangle$ rather than $|\pm\rangle$ [10,33,34] to indicate the majority and minority subbands for easier tracking, as explained in Fig. 2.

B. Adding spin-flip scattering as a leading order inelastic bias-dependence term

We define an electrode-specific phenomenological spin-flip scattering term

$$\Gamma_{ABpq} = \Gamma_{(R,F)(U,D)(du,ud)}. \quad (3)$$

From left to right, the first subscript position $A = (R,F)$ indicates the spin-flip scattering action is occurring with magnon excitation in the R or F layer. The second subscript $B = (U,D)$ describes the upstream and downstream electrodes, as defined by momentum-space direction of tunnel electrons. The third and fourth subscripts describe the direction of spin-flip, with (du) for minority-to-majority band electron scattering, and (ud) for majority-to-minority.

As a leading order expansion from constant tunnel conductance at low bias, assume these Γ_{ABpq} -factors are the only ones with bias- V dependence in conductance. Treat them as the leading order correction to the low-bias elastic tunnel expressions Eq. (2) (i.e. Eqs. (2)-(3) in Ref. [34]). Following Ref. [10,33,34], we derive the subband electrode- and spin-specific conductance. The $G_{\sigma,\sigma'}$ by Eq. (2) with the spin-flip scattering factor Eq. (3) included now reads

$$\begin{aligned} G_{uu} &= \Omega_{Ru}\Omega_{Fu} + \Gamma_{RUdu}\Omega_{Fu}\Omega_{Rd} + \Gamma_{FDud}\Omega_{Ru}\Omega_{Fd}, \\ G_{dd} &= \Omega_{Rd}\Omega_{Fd} + \Gamma_{FDdu}\Omega_{Fu}\Omega_{Rd} + \Gamma_{RUud}\Omega_{Ru}\Omega_{Fd}, \\ G_{ud} &= \Omega_{Ru}\Omega_{Fd} + \Gamma_{RUdu}\Omega_{Fd}\Omega_{Rd} + \Gamma_{FDdu}\Omega_{Ru}\Omega_{Fu}, \\ G_{du} &= \Omega_{Rd}\Omega_{Fu} + \Gamma_{FDud}\Omega_{Fd}\Omega_{Rd} + \Gamma_{RUud}\Omega_{Ru}\Omega_{Fu}. \end{aligned} \quad (4)$$

The subband differential conductances are then computed from spin eigenstate rotation, following the description after Eq. (2) and in Refs. [33,34]:

$$\begin{aligned} g_{Ru} &= G_{uu} \cos^2(\theta/2) + G_{ud} \sin^2(\theta/2), \\ g_{Rd} &= G_{dd} \cos^2(\theta/2) + G_{du} \sin^2(\theta/2), \\ g_{Fu} &= G_{uu} \cos^2(\theta/2) + G_{du} \sin^2(\theta/2), \\ g_{Fd} &= G_{dd} \cos^2(\theta/2) + G_{ud} \sin^2(\theta/2). \end{aligned} \quad (5)$$

The presence of the Γ_{ABpq} s in Eq. (4) through $G_{\sigma\sigma'}$ necessitates the distinction in Eqs. (4)–(5) of upstream vs downstream electrons. Equations (4) and (5) as written above are explicitly coded for the direction of electrons tunnel from reference into the free layer, corresponding to a spin-torque-driven AP-to-P switching direction, or, a “write-0” (W0) direction. The opposite voltage bias direction corresponds to a substitution of subscripts in the form of $\{R, F\} \rightarrow \{F, R\}$ in Eqs. (4) and (5).

The sum $g_{Xu} + g_{Xd}$ for $X \in [F, R]$ in Eq. (5) should and does give the same result as dictated by charge neutrality. It gives the junction’s total differential conductance as $g(\theta) = g_{(R,F)u} + g_{(R,F)d}$. The parallel and antiparallel charge conductances are of course $g(0)$ and $g(\pi)$, respectively. For ease of discussion below, these “collinear” conductances are further written as $g_{\mu W\nu}(V)$. To the leading order of the Γ s, for the two configurations of $\theta = (0, \pi)$ corresponding to $\mu = [0, 1]$, and the two possible bias direction of $\nu = [0, 1]$, it yields

$$\begin{aligned} g_{0W0} &= \Omega_{Fu}[\Omega_{Rd}(\Gamma_{FDdu} + \Gamma_{RUdu}) + \Omega_{Ru}] \\ &\quad + \Omega_{Fd}[\Omega_{Ru}(\Gamma_{FDud} + \Gamma_{RUud}) + \Omega_{Rd}], \\ g_{1W0} &= \Omega_{Rd}[\Omega_{Fd}(\Gamma_{FDud} + \Gamma_{RUdu}) + \Omega_{Fu}] \end{aligned}$$

$$\begin{aligned} &+ \Omega_{Ru}[\Omega_{Ru}(\Gamma_{FDdu} + \Gamma_{RUud}) + \Omega_{Fd}], \\ g_{0W1} &= \Omega_{Fu}[\Omega_{Rd}(\Gamma_{FUud} + \Gamma_{RDud}) + \Omega_{Ru}] \\ &\quad + \Omega_{Fd}[\Omega_{Ru}(\Gamma_{FUdu} + \Gamma_{RDdu}) + \Omega_{Rd}], \\ g_{1W1} &= \Omega_{Rd}[\Omega_{Fd}(\Gamma_{FUud} + \Gamma_{RDud}) + \Omega_{Fu}] \\ &\quad + \Omega_{Ru}[\Omega_{Ru}(\Gamma_{FUud} + \Gamma_{RDdu}) + \Omega_{Fd}]. \end{aligned} \quad (6)$$

The subscripts for $g_{\mu W\nu}$ means “in state μ and in the bias direction for writing to state ν ”.

We then take the leading order expansion of

$$\Gamma_{ABpq} \approx \eta_{ABpq}V, \quad (7)$$

with V being the voltage across the MTJ, now confined to $V \geq 0$, as reverse bias is handled by an R/F index swap, discussed below [Eq. (5)]. η_{ABpq} are the electrode- and subband-specific spin-flip scatter-rate’s voltage dependence slope. It is the average value of the second-order derivative d^2I/dV^2 of the spin subband, similar to what was illustrated earlier in Fig. 1 with a measured MTJ’s IV, but here for spin subbands.

IV. CHARGE CONDUCTANCE

A sum of Eq. (5) in its angular dependent form gives the tunnel differential conductance as

$$g(\theta) = g_A + g_B \cos \theta, \quad (8)$$

with

$$\begin{aligned} g_{A,B} &= \frac{1}{2}[(1 \pm \Gamma_{FDud} \pm \Gamma_{RUdu})\Omega_{Fd}\Omega_{Rd} \\ &\quad \pm (1 \pm \Gamma_{FDdu} \pm \Gamma_{RUud})\Omega_{Fu}\Omega_{Rd} \\ &\quad \pm (1 \pm \Gamma_{FDud} \pm \Gamma_{RUud})\Omega_{Fd}\Omega_{Ru} \\ &\quad + (1 \pm \Gamma_{FDdu} \pm \Gamma_{RUud})\Omega_{Fu}\Omega_{Ru}]. \end{aligned} \quad (9)$$

This expression is for voltage bias as shown in Fig. 2, or for the STT-direction to favor a parallel state. Borrowing a memory-technology term, we name this the “W0” direction of bias. For Eq. (9) to represent the opposite voltage bias direction of “W1”, a substitution of $U \rightarrow D$ needs to be made made.

A. Tunnel magnetoresistance (TMR)

The low-bias voltage limit of Eq. (8), where all $\Gamma_{ABpq} \rightarrow 0$ gives

$$\begin{aligned} g_0(\theta) &= \frac{1}{2}[(\Omega_{Fd} + \Omega_{Fu})(\Omega_{Rd} + \Omega_{Ru})] + \\ &\quad + \frac{1}{2}[(\Omega_{Fd} - \Omega_{Fu})(\Omega_{Rd} - \Omega_{Ru})] \cos \theta. \end{aligned} \quad (10)$$

Write the tunnel density-of-state’s spin-polarization for the R and F electrodes as

$$P_{R,F} = \frac{\Omega_{(R,F)u} - \Omega_{(R,F)d}}{\Omega_{(R,F)u} + \Omega_{(R,F)d}}, \quad (11)$$

which leads to the expression of low-bias tunnel magnetoresistance m_r :

$$m_r = \frac{g_p - g_{ap}}{g_{ap}} = \frac{2P_F P_R}{1 - P_F P_R}, \quad (12)$$

where $g_p = g_0(0)$, and $g_{ap} = g_0(\pi)$. $P_{R,F}$ are the density-of-state spin-polarization factors of the R, F electrodes.

A corresponding evaluation of $(g_p - g_{ap})/g_{ap}$ including the Γ_{ABpq} s gives the leading-order bias-dependence of TMR.

B. Bias-dependent IV and spin-flip scatter

In this simplified approach, we assume the leading contributor to the bias dependence of our MTJ comes from inelastic events related to spin-flip scatter. It then allows us to define a set of observation-based, measurable bias-dependent reduced conductance as

$$\begin{aligned}\Gamma_{0W0} &= \frac{g_{0W0}(V) - g_{0W0}(0)}{g_{1W0}(0)}, \\ \Gamma_{1W0} &= \frac{g_{1W0}(V) - g_{1W0}(0)}{g_{0W0}(0)}, \\ \Gamma_{0W1} &= \frac{g_{0W1}(V) - g_{0W1}(0)}{g_{1W1}(0)}, \\ \Gamma_{1W1} &= \frac{g_{1W1}(V) - g_{1W1}(0)}{g_{0W1}(0)},\end{aligned}\quad (13)$$

where $g_{0W\nu}(0) = g_p$, $g_{1W\nu}(0) = g_{ap}$ are the low-bias conductances for P and AP states.

Equation (13) are the net differential conductance increases at elevated bias, cross-normalized to the zero-bias conductance of the opposite orientation. They are in the same form as the empirical relation Eq. (1) discussed earlier, except for using the $\mu W \nu$ notation for representing the four combinations of (collinear) moment and bias directions.

Discussions in Sec. 1 surrounding Eq. (1) give experimental observations stating that (1) $\Gamma_{\mu W \nu} \approx \eta_{\mu W \nu} V$ are mostly V-proportional; and (2) they lead to a range of $\eta_{\mu W \nu}$ values around 0.1 to 1 (1/V) [28]. The $\eta_{\mu W \nu}$ can be viewed as the voltage mean-value of the second-order differential conductance d^2I/dV^2 . Using $\eta_{\mu W \nu}$ together with Eq. (6), one could express the reduced conductances in Eq. (13) in terms of electrode-specific spin-flip scatter rate's voltage slopes. Namely,

$$\begin{aligned}\eta_{0W0} &= \frac{(\eta_{FDdu} + \eta_{RUdu})\Omega_{Fu}\Omega_{Rd} + (\eta_{FDud} + \eta_{RUud})\Omega_{Fd}\Omega_{Ru}}{\Omega_{Fu}\Omega_{Rd} + \Omega_{Fd}\Omega_{Ru}}, \\ \eta_{1W0} &= \frac{(\eta_{FDud} + \eta_{RUdu})\Omega_{Fd}\Omega_{Rd} + (\eta_{FDdu} + \eta_{RUud})\Omega_{Fu}\Omega_{Ru}}{\Omega_{Fd}\Omega_{Rd} + \Omega_{Fu}\Omega_{Ru}}, \\ \eta_{0W1} &= \frac{(\eta_{FUud} + \eta_{RDud})\Omega_{Fu}\Omega_{Rd} + (\eta_{FUdu} + \eta_{RDdu})\Omega_{Fd}\Omega_{Ru}}{\Omega_{Fu}\Omega_{Rd} + \Omega_{Fd}\Omega_{Ru}}, \\ \eta_{1W1} &= \frac{(\eta_{FUdu} + \eta_{RDud})\Omega_{Fd}\Omega_{Rd} + (\eta_{FUud} + \eta_{RDdu})\Omega_{Fu}\Omega_{Ru}}{\Omega_{Fd}\Omega_{Rd} + \Omega_{Fu}\Omega_{Ru}}.\end{aligned}\quad (14)$$

This relationship can be solved to deduce the electrode-specific η_{XYpq} from the measured $\eta_{\mu W \nu}$ under some simplifying assumptions.

V. SPIN DIFFERENTIAL CONDUCTANCE AND SPIN-TORQUE

The total spin current at the tunnel barrier interface can be found by considering the pill-box around the electrode interface at the tunnel barrier, as illustrated by the dashed line box in Fig. 2. Unit vectors \mathbf{n}_R and \mathbf{n}_F represent the

magnetic moment direction of R and F layers respectively; \mathbf{e}_{R_p} and \mathbf{e}_{F_p} are unit vectors representing the transverse in-plane directions. We do not include the so-called out-of-plane, or field-like torque term [36] in this analysis.

Assuming the tunnel barrier has no spin-flip scatter centers, one can write down the angular momentum conservation relation for spin-current flowing into and out of the pill-box region in Fig. 2. This gives, for transverse (in-plane) spin-torque of the R and F layer moments $\mathbf{T}_{p(R,F)} = T_{p(R,F)}\mathbf{e}_{(R_p,F_p)}$:

$$\mathbf{T}_{pR} + \mathbf{T}_{pF} = \left(\frac{\hbar}{2e}\right)[(I_{Ru} - I_{Rd})\mathbf{n}_R + (I_{Fu} - I_{Fd})\mathbf{n}_F], \quad (15)$$

where $I_{(R,F)(u,d)}$ represents the majority and minority subchannel electron current for the R and F layers.

A voltage derivative on both sides of Eq. (15) gives the in-plane ‘‘torqance’’ [33] $\boldsymbol{\tau}_{p(R,F)} = d\mathbf{T}_{p(R,F)}/dV$ on the left-hand side, and the subchannel differential conductance pieces [Eq. (5)] on the right-hand side. That is

$$\boldsymbol{\tau}_{pR} + \boldsymbol{\tau}_{pF} = \left(\frac{\hbar}{2e}\right)[(g_{Ru} - g_{Rd})\mathbf{n}_R + (g_{Fu} - g_{Fd})\mathbf{n}_F], \quad (16)$$

which solves to give²

$$\begin{aligned}\tau_{pR} &= \left(\frac{\hbar}{4e}\right)[\Omega_{Fu}(1 - \Gamma_{FDdu}) - \Omega_{Fd}(1 - \Gamma_{FDud}) \\ &\quad [\Omega_{Ru}(1 + \Gamma_{RUud}) + \Omega_{Rd}(1 + \Gamma_{RUdu})] \sin \theta, \\ \tau_{pF} &= \left(\frac{\hbar}{4e}\right)[\Omega_{Fu}(1 + \Gamma_{FDdu}) + \Omega_{Fd}(1 + \Gamma_{FDud}) \\ &\quad [\Omega_{Ru}(1 - \Gamma_{RUud}) - \Omega_{Rd}(1 - \Gamma_{RUdu})] \sin \theta.\end{aligned}\quad (17)$$

A voltage integration of $\tau_{p(R,F)}$ from Eq. (17) gives the in-plane transverse spin-torque

$$T_{p(R,F)} = \int_0^V \tau_{p(R,F)} dV. \quad (18)$$

Spin-flip scattering introduces a spin-current in the form of magnons whose polarization remains collinear with that of the electrodes, as long as the magnons involved in spin-flip scatter are incoherent. Tallying up each spin-flip scatter term in the charge transport equation for $g(\theta) = g_{Ru} + g_{Rd} = g_{Fu} + g_{Fd}$ gives its corresponding electrode's magnon spin-current differential conductance in the form of

$$\begin{aligned}g_{Rm} &= [(\Omega_{Fu} + \Omega_{Fd})(\Gamma_{RUud}\Omega_{Ru} - \Gamma_{RUdu}\Omega_{Rd}) + \\ &\quad + [(\Omega_{Fd} - \Omega_{Fu})(\Gamma_{RUud}\Omega_{Ru} + \Gamma_{RUdu}\Omega_{Rd})] \cos \theta, \\ g_{Fm} &= [(\Omega_{Ru} + \Omega_{Rd})(\Gamma_{FDud}\Omega_{Fd} - \Gamma_{FDdu}\Omega_{Fu}) - \\ &\quad - [(\Omega_{Rd} - \Omega_{Ru})(\Gamma_{FDud}\Omega_{Fd} + \Gamma_{FDdu}\Omega_{Fu})] \cos \theta.\end{aligned}\quad (19)$$

The voltage-integration of $g_{(R,F)m}$ in spin unit gives the total magnon spin current as

$$I_{(R,F)ms} = \left(\frac{\hbar}{2e}\right) \int_0^V g_{(R,F)m} dV. \quad (20)$$

These expressions above, Eqs. (15)–(20), are specific to spin-torque current polarity corresponding to driving an AP-to-P, or write-0 (‘‘W0’’) transition. For the opposite polarity, a

²Eq. (17) to be taken to the leading (first) order of Γ_{ABpq} only.

{“R”→“F”, “F”→“R”} substitution in the above Eqs. (15)–(17) and Eq. (19) is needed.

VI. TORQUE AND MAGNON CURRENTS UNDER SIMPLIFYING APPROXIMATIONS

These general expressions shown above contain too many unknown parameters for direct comparison with experiments. Below, we consider two specific approximation cases, where the number of parameters is reduced to a manageable level.

Two intuitive approach to the reduction of scatter parameters are (1) assuming upstream spin-flip rates are much lower than that of the downstream, as upstream tunnel electrons dynamics occur at the Fermi level, whereas downstream electrons are V_w above, giving rise to strongly V-dependent scatter rate; and (2) the “du” (or down-to-up) scatter rate is likely higher than “ud” for temperatures well below the magnetic ordering exchange energy.

Another simplification method is to examine MTJs with symmetric RL and FL interfaces with the MgO barrier, so that the density-of-state (DOS) related spin-polarizations can be treated as symmetric.

Below, we examine these approximation in combination to reach some quantitative estimates possible for experimental comparison.

A. Case I. Low-temperature, symmetric spin-polarization for both electrodes

In case I, we assume only low-temperature limit, where $\Gamma_{XYdu} \gg \Gamma_{XYud} \rightarrow 0$ for $X \in [R, F]$, and $Y \in [U, D]$. We also assume a nearly symmetric electrode spin-polarization, that is $P_R \approx P_F \approx P$. The spin-flip scatter rates are assumed to be different for the R, F electrodes, and we allow a non-negligible upstream spin-flip scatter rate $\Gamma_{XUdu} = \eta_{XUdu}V$. That is with $\eta_{XUdu} > 0$ for $X \in (R, L)$.

Under these assumptions, one has

$$\begin{aligned} \Omega_d &= \frac{1-P}{1+P} \Omega_u, \\ m_r &= \frac{2P^2}{1-P^2}, \\ g_p &= \frac{2(1+P^2)}{(1+P)^2} \Omega_u^2. \end{aligned} \quad (21)$$

In the case I limit, the spin-torque and magnon spin-current expressions from Eq. (17) and Eq. (19) can be simplified to

$$\begin{bmatrix} \eta_{0W0} \\ \eta_{1W0} \\ \eta_{0W1} \\ \eta_{1W1} \end{bmatrix} = \frac{1}{2(1+P^2)} \begin{bmatrix} 1+P^2 & 1+P^2 & 0 & 0 \\ (1+P)^2 & (1-P)^2 & 0 & 0 \\ 0 & 0 & 1+P^2 & 1+P^2 \\ 0 & 0 & (1+P)^2 & (1-P)^2 \end{bmatrix} \begin{bmatrix} \eta_{FDdu} \\ \eta_{RUdu} \\ \eta_{RDdu} \\ \eta_{FUdu} \end{bmatrix}. \quad (25)$$

The use for case I approximation is, for such symmetric junction electrodes, one should be able to establish an upper limit for the amount of upstream spin-flip scatter that is likely to be present in these structures. Once confirmed by experiments that the upstream spin-flip scatter rate is likely far lower

read

$$\begin{aligned} \tau_{pR, W0} &\approx \tau_0 \left[1 - \frac{(1+P)\eta_{FDdu} - P(1-P)\eta_{RUdu}}{2P} V \right], \\ \tau_{pR, W1} &\approx \tau_0 \left[1 - \frac{P(1+P)\eta_{FDdu} + (1-P)\eta_{RUdu}}{2P} V \right], \\ \tau_{pF, W0} &\approx \tau_0 \left[1 + \frac{(1-P)\eta_{FUdu} + P(1-P)\eta_{RDdu}}{2P} V \right], \\ \tau_{pF, W1} &\approx \tau_0 \left[1 + \frac{P(1-P)\eta_{FUdu} - (1+P)\eta_{RDdu}}{2P} V \right], \end{aligned} \quad (22)$$

where $\tau_0 = \frac{P}{1+P^2} \left(\frac{\hbar}{2e} \right) g_p \sin \theta$ is the elastic spin-torque expression.

The corresponding magnon differential spin-conductance can be written as

$$\begin{aligned} g_{RmW0} &\approx -g_p \left(\frac{1-P}{1+P^2} \right) (1+P \cos \theta) \eta_{RUdu} V, \\ g_{RmW1} &\approx -g_p \left(\frac{1+P}{1+P^2} \right) (1-P \cos \theta) \eta_{RDdu} V, \\ g_{FmW0} &\approx -g_p \left(\frac{1+P}{1+P^2} \right) (1-P \cos \theta) \eta_{FDdu} V, \\ g_{FmW1} &\approx -g_p \left(\frac{1-P}{1+P^2} \right) (1+P \cos \theta) \eta_{FUdu} V, \end{aligned} \quad (23)$$

and the electrode-specific η_{XYpq} expressed in measured $\eta_{\mu Wv}$ follows, from Eq. (14), (21):

$$\begin{aligned} \eta_{RUdu} &= \frac{(1+P)^2 \eta_{0W0} - (1+P^2) \eta_{1W0}}{2P}, \\ \eta_{RDdu} &= \frac{(1+P^2) \eta_{1W1} - (1-P)^2 \eta_{0W1}}{2P}, \\ \eta_{FUdu} &= \frac{(1+P)^2 \eta_{0W1} - (1+P^2) \eta_{1W1}}{2P}, \\ \eta_{FDdu} &= \frac{(1+P^2) \eta_{1W0} - (1-P)^2 \eta_{0W0}}{2P}. \end{aligned} \quad (24)$$

The case I assumption is likely only for very limited experimental cases where one could claim symmetric tunnel density of states for electrodes on either side of the tunnel barrier. Once one deviates from that (with dissimilar electrodes at the interface for R and F), the case I assumption is no longer valid.

The case I relationship between $\eta_{\mu Wv}$ and η_{XYpq} can also be written in matrix form which reads

than that of the downstream, one could employ the case II approximation with more confidence.

One challenge of this approach may lie in the strong dependence of η_{XUdu} on η_{0Wv} , which appears for high MR junctions to have a lot more variations, some with bias-V dependent

features in $\Gamma(V)$ in addition to the linear- V dependence. The exact causes of these variability is still under investigation, it may well be related to interface composition and texture dependent band-structure-related conductance variations in Ref. [13] and further discussed in the Supplemental Material [31]. Such variability makes the deduction of η_{XUdu} less reliable than that of η_{XDdu} , which is more strongly dependent on η_{1Wv} , and which has less variability experimentally.

B. Case II. Asymmetric spin-polarization for electrodes, assuming no upstream spin-flip scatter

In case II, we assume asymmetric spin-polarizations for R and F electrodes, but neglect upstream spin-flip scatter terms, i.e., let $\Gamma_{XUdu} \rightarrow 0$ for $X \in (R, L)$. These give

$$\begin{aligned}\Omega_{(R,F)d} &= \frac{1 - P_{(R,F)}}{1 + P_{(R,F)}} \Omega_{(R,F)u}, \\ m_r &= \frac{2P_F P_R}{1 - P_F P_R}, \\ g_p &= \frac{2(1 + P_F P_R)}{(1 + P_F)(1 + P_R)} \Omega_{Fu} \Omega_{Ru}.\end{aligned}\quad (26)$$

The case II spin-torques within low-temperature limit of $\Gamma_{XYdu} \gg \Gamma_{XYud} \rightarrow 0$ read

$$\begin{aligned}\tau_{pR,W0} &\approx \tau_1 \left(\frac{2P_F}{1 + P_F P_R} \right) \left[1 - \left(\frac{1 + P_F}{2P_F} \right) \eta_{FDdu} V \right], \\ \tau_{pR,W1} &\approx \tau_1 \left(\frac{2P_F}{1 + P_F P_R} \right) \left[1 + \left(\frac{1 + P_R}{2} \right) \eta_{RDdu} V \right], \\ \tau_{pF,W0} &\approx \tau_1 \left(\frac{2P_R}{1 + P_F P_R} \right) \left[1 + \left(\frac{1 + P_F}{2} \right) \eta_{FDdu} V \right], \\ \tau_{pF,W1} &\approx \tau_1 \left(\frac{2P_R}{1 + P_F P_R} \right) \left[1 - \left(\frac{1 + P_R}{2P_R} \right) \eta_{RDdu} V \right],\end{aligned}\quad (27)$$

with $\tau_1 = (\hbar/4e)g_p \sin \theta$ defines the prefactor.

The effect of a voltage-dependent spin-flip scattering process effectively changes the apparent tunnel density-of-states of the electrode underwent such spin-flip scattering. That is why the FL torque is voltage modified by the RL P_R and vice versa [33]. The sign of the voltage term reflects the effect of such a term on the overall electron-transported angular momentum. A minority-band dominant spin-flip scattering reduces the torque (as in the case of W1), whereas a majority-band dominant spin-flip enhances the torque. The same can be observed in Eq. (22) for case I, albeit with a somewhat more complex form.

The corresponding magnon spin-conductance expressions are

$$\begin{aligned}g_{RmW0} &\approx 0, \\ g_{RmW1} &\approx -g_p \left(\frac{1 + P_R}{1 + P_F P_R} \right) (1 - P_F \cos \theta) \eta_{RDdu} V, \\ g_{FmW0} &\approx -g_p \left(\frac{1 + P_F}{1 + P_F P_R} \right) (1 - P_R \cos \theta) \eta_{FDdu} V, \\ g_{FmW1} &\approx 0.\end{aligned}\quad (28)$$

There is also a corresponding translation between the measured $\eta_{\mu Wv}$ and electrode-specific η_{XDdu} for $X \in [R, F]$. From

Case II: F-layer transverse spin-torque vs bias voltage

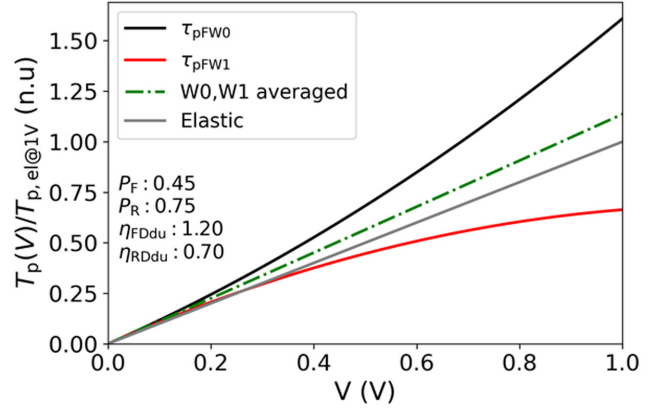


FIG. 3. An illustration of the transverse spin-torque on F layer as $\tau_{pF,W0,1}$ in case II limit. The parameters used are listed in the figure. The reduced spin-torque vs bias (normalized by the elastic term) is calculated using Eqs. (27) and (18).

Eqs. (14), and (26), and assuming $P_R \rightarrow 1$:³

$$\begin{aligned}\eta_{FDdu} &\approx \eta_{1W0}, \\ \eta_{RDdu} &\approx \frac{(1 + P_F)^2 \eta_{1W1} - (1 - P_F)^2 \eta_{0W1}}{4P_F},\end{aligned}\quad (29)$$

with $P_F = m_r/P_R^2(2 + m_r)$ and $P_R \sim 1$ one could calculate an MTJ's electrode specific spin-flip scatter rate slope, and thereby assess its electrode's magnetic state at MgO tunnel barrier interface.

One may also express $\eta_{\mu Wv}$ in terms of η_{XYpq} . These follow from Eq. (14). For case II and high $P_R = 1 - \epsilon$ with $\epsilon \ll 1$ but a nonunity $P_F < 1$ gives

$$\begin{aligned}\eta_{0W0} &\approx \eta_{FDdu} + \epsilon \frac{(1 + P_F)(\eta_{FDdu} - \eta_{FDud})}{2(1 - P_F)}, \\ \eta_{1W0} &\approx \eta_{FDdu} - \epsilon \frac{(1 - P_F)(\eta_{FDdu} - \eta_{FDud})}{2(1 + P_F)}, \\ \eta_{0W1} &\approx \eta_{RDdu} - \epsilon \frac{(1 + P_F)(\eta_{RDdu} - \eta_{RDud})}{2(1 - P_F)}, \\ \eta_{1W1} &\approx \eta_{RDdu} + \epsilon \frac{(1 - P_F)(\eta_{RDdu} - \eta_{RDud})}{2(1 + P_F)},\end{aligned}\quad (30)$$

which makes η_{0W0} especially sensitive to the details of P_F as its leading term itself η_{FDdu} is likely small compared to other η_{XYpq} s.

VII. DISCUSSION

A. Spin-flip scattering and transverse spin-torque

For the two switchable configurations of ${}^1_0W_1^0$, spin-flip causes downstream STT-switching torque to increase from its elastic linear V -dependence limit, and upstream switching torque to decrease. This can be seen in both cases I and II

³For simplicity, we skipped the expressions for $P_R < 1$, and those for η_{XDdu} which are cumbersome. Further, they are sensitive to $P_{R,F}$, making their extraction from measured $\eta_{\mu W\mu}$ unreliable.

in Eqs. (22) and (27). An illustration with the case II limit is shown in Fig. 3. This illustrates the effect of magnon excitation in the F layer is to enhance the W0 spin-torque on F layer, whereas the excitation in R layer goes to reduce W1 spin-torque on the F layer, due to reduced net magnetic polarization. The spin-flip scatter parameters used in Fig. 3 are representative values consistent with our experiments. Thus spin-flip scattering in MTJs should have observable effects on dissipative spin-torque, especially at higher bias voltage end around 0.5 V or so. This mechanism would result in more efficient switching at high bias for W0, and less efficient high-bias switching for W1.

B. Spin-flip scattering and magnon spin-current

Spin-flip scattering generated magnon spin-current can be estimated with Eqs. (23) and (28) for our two simplified cases also. For comparison with magnetic moment related discussions, it is often convenient to write the magnon current in Bohr magnetons. Through Eq. (20), the magnon spin-current can be converted to Bohr-magneton current, and be used to estimate the amount of magnetic moment reduction.

For case II, combining Eq. (28) with (20) gives a magnon moment current of the form for F layer and in the “1W0” direction a magnon magnetic moment current of $I_{Fm1W0} = \epsilon_{F1W0} V^2$, with

$$\epsilon_{F1W0} \approx g_p \left(\frac{\mu_B}{e} \right) \frac{(1 + P_F)(1 + P_R)}{2(1 + P_F P_R)} \eta_{FDdu}. \quad (31)$$

Note $I_{Fm0W1} = 0$ in the case II limit.

C. Spin-flip scattering related magnon numbers

The added magnon excitation from I_{Fm1W0} increases the number of magnons n_{Fm} from its thermal equilibrium value. Assume a near thermal distribution with a relaxation rate of τ_{Fm} , and if the added magnon number density per unit area in the F layer due to the magnon generation current is n_{Fm} , then

$$\frac{dn_{Fm}}{dt} = -\frac{n_{Fm}}{\tau_{Fm}} + \frac{|I_{Fm}|}{2\mu_B} \rightarrow 0, \quad (32)$$

in steady state. This gives n_{Fm} in I_{Fm} and τ_{Fm} as

$$n_{Fm} \approx \left(\frac{\tau_{Fm}}{2\mu_B} \right) I_{Fm} \approx \left(\frac{\tau_{Fm}}{2\mu_B} \right) \epsilon_{F1W0} V_w^2. \quad (33)$$

The value of τ_{Fm} is not well known. If the magnon-magnon scattering relaxation speed is faster than magnon-lattice relaxation, it is possible for the additional hot-electron-generated magnons to condense at the low-energy end of the magnon dispersion spectrum. On the other hand, if the magnon-magnon relaxation speed is comparable or slow compared to magnon-lattice, one expect a nearly thermal distribution, with a slightly elevated magnon bath temperature.

For the former scenario, one expects a τ_{Fm} of the order of $1/\alpha\omega_k$ with $k \rightarrow \pi/a$ where a is the MTJ diameter. That could result in some very long-living magnon states with $\tau_{Fm} \sim 0.1$ to 1 ns, dominated by the low-lying standing wave energy.

If it is the later scenario, then τ_{Fm} is associated with a frequency comparable to $k_B T$. If ambient temperature and $\alpha \approx 0.01$, then $\tau_{Fm} \approx h/k_B T \alpha \approx 16$ ps.

Using Eq. (33), one gets an estimate of the magnons generated by the spin-flip scattering tunnel electrons. Converting it to effective magnetic moment-thickness product (so as to render it a per unit area quantity, where t is film thickness of the FL electrode), the net reduction of the FL's saturation magnetization by the amount of $M_{\text{seff}} = M_s - M_{\text{st}}$, and

$$M_{\text{st}} = 2\mu_B n_{Fm} \approx \tau_{Fm} \epsilon_{F1W0} V_w^2, \quad (34)$$

or equivalently

$$M_{\text{seff}} \approx M_s \left[1 - \left(\frac{\tau_{Fm} \epsilon_{F1W0}}{M_s t} \right) V_w^2 \right]. \quad (35)$$

This relation can be compared with experiment. Note the bias dependence of Eq. (35) is of the same form as if the F layer moment is being reduced by Joule heating, even though here the reduction is not due to increased thermal magnons but originates from hot-electron spin-flip scattering induced incoherent magnons.

Within the assumptions of case II, there is no upstream spin-flip scattering, consequently, $\epsilon_{F0W1} = 0$.

VIII. COMPARISON WITH EXPERIMENTS

In real-life device structures, there are other factors influencing switching asymmetry, including band-structure effects (discussed extensively above and in the Supplemental Material [31]), Joule heating [37,38], chirality-dependent dynamic dipolar coupling between F layer and R layer [39], voltage-induced perpendicular anisotropy change [40–42], and other more subtle effects such as edge- vs center-nucleation of reversal volume when the MTJ diameter is comparable or larger than layer's exchange length, and high-frequency interface magnetodynamics [29,43]. It is often nontrivial to isolate individual contributions to spin-flip scattering related effects.

We now examine experimental data for comparison with major model expectations using our perpendicularly magnetized (PMA) MTJs of CoFeB | MgO | CoFeB type [44,45]. These MTJs have their thin-film stacks similar to Ref. [46,47]. Films are based on a ~ 1.7 nm thick CoFeB free-layer (F), and a synthetic antiferromagnetic (SAF) reference layer (R), sputter deposited at ambient temperature, followed by a vacuum anneal around 300–400 °C for 1 h prior to fabrication. Device diameter ranges from 15–150 nm as estimated from resistance, and selectively calibrated via scanning electron microscopy. Tunnel magnetoresistance is of the order $\sim 100\%$. The resistance-area product (RA, or r_A) ranges from ~ 5 to $30 \Omega \mu\text{m}^2$. For investigation on the roles of tunnel barrier facing F-layer magnetic properties, various dopants are introduced in sub-Ångstrom form into the F layer.

We take a case II limit, which assumes asymmetric $P_{R,F}$ and with the simplifying assumption of $P_R \rightarrow 1$ and m_r directly relates to P_F , as discussed below [Eq. (29)], and as discussed in the section above. This is an approximation to reduce the number of materials parameters. It is justified by the sample set in this study, where the RL is kept with the same design that is known to give TMR $\gg 100\%$ for simple CoFeB electrodes, whereas the FL is studied with materials modifications such as interface element doping.

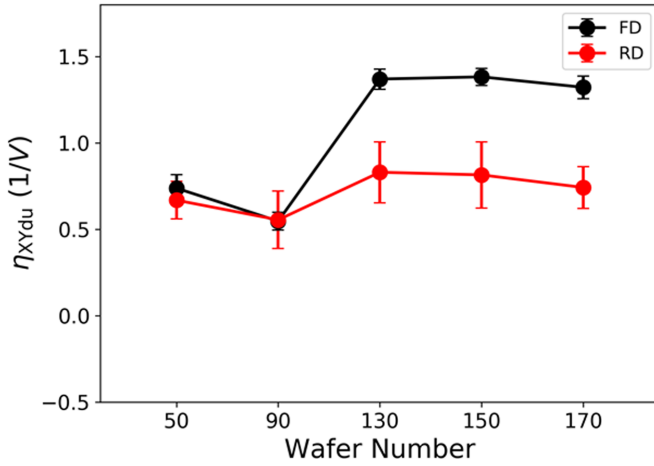


FIG. 4. r_A and interface doping varied set of MTJs' spin-flip scattering coefficient as deduced from their IV curves and through Eq. (29) with the case II assumption discussed in the text, for η_{XYdu} with $XY \in [FD, RD]$

Figure 4 shows results of junctions from five different sample wafers. About 100 junctions from each wafer in the size range between approximately 30 to 40 nm are analysed using their IV curve deduced FL and RL spin-flip scatter rate coefficient as defined by Eq. (29). The samples are from two groups, each with an intentional r_A change by different MgO barrier thicknesses. Wafers 50 and 90 have $r_A \approx 10$ and $20 \Omega\mu\text{m}^2$, respectively, whereas wafers 130, 150, and 170 have $r_A \approx 9$, 12, and, 19 $\Omega\mu\text{m}^2$. The first group of Wafers 50 and 90 have a simple MgO | 1.8nm CoFeB | cap tunnel barrier interface, whereas for wafers 130, 150, and 170, the FL interface has the nominal structure of MgO | 0.1nm V | 1.8nm CoFeB | cap.

Two observations can be made for these two groups of samples. (1) The IV-deduced η_{FDdu} is insensitive to the variations of MTJ r_A as it is tuned by MgO barrier thickness, and (2) The value of η_{FDdu} is *very* sensitive to 1 Å of vanadium doping at the MgO-CoFeB interface⁴. As discussed above, $\eta_{FDdu} \propto 1/A_{exF}$ with A_{exF} representing the FL's tunnel barrier interface region exchange energy. The correlation between interface vanadium doping and an increase in η_{FDdu} is consistent with V-doping's effect of reducing ferromagnetic coupling.

The values of η_{RDdu} appear to be less sensitive to either r_A change or doping. This is consistent with the constant lower interface structure at the RL | MgO interface. The small rise of η_{RDdu} upon FL V-doping should probably not be taken seriously, as our case II assumption is relatively crude in terms of describing real-life experimental data.

To more directly probe the strength of spin-torque the FL receives during switching, we also examined another experimental sample set including a RL design similar to the one mentioned above, while the FL's doping is varied. We use the write-error's inverse log-linear slope against write voltage as a proxy for the strength of spin-torque [48–51]. The ratio of the

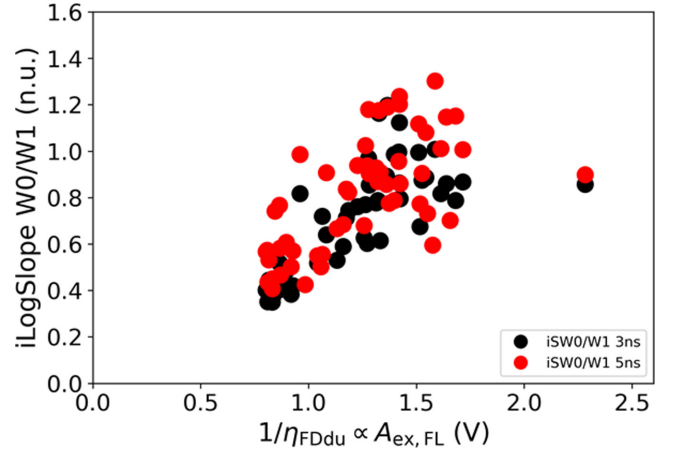


FIG. 5. Experimental measurement of various tunnel devices with different FL composition. The measured inverse write-error slope of $\delta V_w / \delta \log_{10} \epsilon_r$ is plotted against $1/\eta_{FDdu}$ from the same junction's IV curve using Eq. (29). Each data point is an average from $\sim 10^2$ junctions from the same layer structure and size-group on the same wafer and location. The sizes examined in this dataset is restricted to 25 to 35 nm in diameter. Data are presented with two different switching pulse widths at 3 and 5 ns.

resulting write error rate's inverse log slopes (WER slope, in unit of mV/decade of error reduction) from the W0/W1 directions [49] using two different write-pulse widths (3 and 5 ns) are plotted against the same junction IV-deduced $1/\eta_{FD} \propto A_{exF}$. We see the WER slope's W0/W1 slope ratio increases in value when the corresponding junction's IV-deduced FL interface $A_{ex,F} \propto 1/\eta_{FDdu}$ increases, as illustrated in Fig. 5.

These results suggest for enhanced FL spin-flip scatter rate η_{FDdu} , corresponding to a weakened FL-barrier interface magnetic exchange energy, there is a corresponding increase in W0 direction switching efficiency, or a steeper switching write-error slope with fewer mV/decade for error reduction. This is consistent qualitatively in trend as one would expect from the discussions surrounding Fig. 3, providing experimental evidence that a spin-flip scattering mediated nonlinear spin-torque effect is at play.

IX. CONCLUSIONS

Spin-flip scattering due to hot tunnel electrons in an spin-torque switched MTJ results in asymmetric spin-torque in “0W1” and “1W0” directions, giving relatively higher antidamping torque at elevated bias for the 1W0 direction than to 0W1. Among many other mechanisms contributing to W0/W1 asymmetries in an MTJ for memory applications, such spin-flip scattering contribution makes it relatively harder for “0W1” switch at high speed (i.e. high bias V_w) compared to “1W0” for typical MTJs with MgO-barrier and a CoFeB-like ferromagnetic electrodes. Spin-flip scattering also leads to a reduction of moment on the F-layer side in “1W0” direction, and an R-layer moment reduction in “0W1” direction. A correlation between IV-deduced spin-flip scatter rate as signified by a “cross-normalized” conductance vs bias slope and that of switching W0/W1 asymmetry is expected, consistent with experimental observations in our data.

⁴Describing the ambient temperature film deposition sequence, and not necessarily reflective of the final elemental position state upon postdeposition annealing.

ACKNOWLEDGMENTS

Experimental work done with the MRAM group at IBM T. J. Watson Research Center supported in part by partnership with Samsung Electronics. I particularly acknowledge E. R. J.

Edwards, M. Gottwald, G. Hu, P. Hashemi, G. Lauer, J. J. I. Nowak, P. L. Trouilloud, and D. C. Worledge for conducting related experiments and for making experimental data available for this analysis.

-
- [1] S. Zhang, P. M. Levy, A. C. Marley, and S. S. P. Parkin, *Phys. Rev. Lett.* **79**, 3744 (1997).
- [2] R. Vollmer, M. Etzkorn, P. S. A. Kumar, H. Ibach, and J. Kirschner, *Phys. Rev. Lett.* **91**, 147201 (2003).
- [3] Y. Lu, M. Tran, H. Jaffrès, P. Seneor, C. Deranlot, F. Petroff, J.-M. George, B. Lépine, S. Ababou, and G. Jézéquel, *Phys. Rev. Lett.* **102**, 176801 (2009).
- [4] P. M. Levy and A. Fert, *Phys. Rev. B* **74**, 224446 (2006).
- [5] D. Bang *et al.*, *J. Appl. Phys.* **105**, 07C924 (2009).
- [6] T. Balashov, A. F. Takacs, M. Dane, A. Ernst, P. Bruno, and W. Wulfhekel, *Phys. Rev. B* **78**, 174404 (2008).
- [7] P. Guo, D. L. Li, J. F. Feng, H. Kurt, G. Q. Yu, J. Y. Chen, H. X. Wei, J. M. D. Coey, and X. F. Han, *J. Appl. Phys.* **116**, 153905 (2014).
- [8] C. H. Shang, J. Nowak, R. Jansen, and J. S. Moodera, *Phys. Rev. B* **58**, R2917(R) (1998).
- [9] P. G. Mather, A. C. Perrella, E. Tan, J. C. Read, and R. A. Buhrman, *Appl. Phys. Lett.* **86**, 242504 (2005).
- [10] J. C. Slonczewski and J. Z. Sun, *J. Magn. Magn. Mater.* **310**, 169 (2007).
- [11] J. R. Kirtley and D. J. Scalapino, *Phys. Rev. Lett.* **65**, 798 (1990).
- [12] C. Heiliger and M. D. Stiles, *Phys. Rev. Lett.* **100**, 186805 (2008).
- [13] C. Franz, M. Czerner, and C. Heiliger, *Phys. Rev. B* **88**, 094421 (2013).
- [14] J. Z. Sun, D. W. Abraham, K. Roche, and S. S. P. Parkin, *Appl. Phys. Lett.* **73**, 1008 (1998).
- [15] Y. Lu, X. W. Li, G. Xiao, R. A. Altman, W. J. Gallagher, A. Marley, K. Roche, and S. Parkin, *J. Appl. Phys.* **83**, 6515 (1998).
- [16] H. Sukegawa, H. Xiu, T. Ohkubo, T. Furubayashi, T. Niizeki, W. Wang, S. Kasai, S. Mitani, K. Inomata, and K. Hono, *Appl. Phys. Lett.* **96**, 212505 (2010).
- [17] Y. Sakuraba, M. Hattori, M. Oogane, Y. Ando, H. Kato, and A. Miyazaki, *Appl. Phys. Lett.* **88**, 192508 (2006).
- [18] J. Zhang and R. M. White, *J. Appl. Phys.* **83**, 6512 (1998).
- [19] S. S. P. Parkin, C. Kaiser, A. Panchula, P. M. Rice, B. Hughes, M. Samant, and S.-H. Yang, *Nat. Mater.* **3**, 862 (2004).
- [20] D. D. Djayaprawira, K. Tsunekawa, M. Nagai, H. Maehara, S. Yamagata, N. Watanabe, S. Yuasa, Y. Suzuki, and K. Ando, *Appl. Phys. Lett.* **86**, 092502 (2005).
- [21] S. Yuasa, T. Nagahama, A. Fukushima, and Y. S. K. Ando, *Nat. Mater.* **3**, 868 (2004).
- [22] G. D. Fuchs, J. A. Katine, S. I. Kiselev, D. Mauri, K. S. Wooley, D. C. Ralph, and R. A. Buhrman, *Phys. Rev. Lett.* **96**, 186603 (2006).
- [23] S. Ikeda, J. Hayakawa, Y. M. Lee, R. Sasaki, T. Matsukura, and H. Ohno, *Jpn. J. Appl. Phys.* **44**, L1442 (2005).
- [24] J. Hayakawa, S. Ikeda, F. Matsukura, and H. Takahashi, and H. Ohno, *Jpn. J. Appl. Phys.* **44**, L587 (2005).
- [25] F. Greullet, E. Snoeck, C. Tiusan, M. Hehn, D. Lacour, O. Magen, and L. Calmels, *Appl. Phys. Lett.* **92**, 053508 (2008).
- [26] W. Wang, H. Sukegawa, R. Shan, S. Mitani, and K. Inomata, *Appl. Phys. Lett.* **95**, 182502 (2009).
- [27] H. D. Gan, S. Ikeda, W. Shiga, J. Hayakawa, K. Miura, H. Yamamoto, H. Hasegawa, F. Matsukura, T. Ohkubo, K. Hono, and H. Ohno, *Appl. Phys. Lett.* **96**, 192507 (2010).
- [28] J. Z. Sun, P. L. Trouilloud, G. P. Lauer, and P. Hashemi, *AIP Adv.* **9**, 015002 (2019).
- [29] J. Z. Sun, *Phys. Rev. B* **96**, 064437 (2017).
- [30] E. L. Wolf, *Principles of Electron Tunneling Spectroscopy*, (Oxford University Press, Oxford, 1995), Sec. 10.3, p. 437.
- [31] See Supplemental Material at <http://link.aps.org/supplemental/10.1103/PhysRevB.103.094439> for comparing our MTJ's ambient bias dependent IV and spin-torque with those from ab initio calculations.
- [32] J. C. Slonczewski, *Phys. Rev. B* **39**, 6995 (1989).
- [33] J. C. Slonczewski, *Phys. Rev. B* **71**, 024411 (2005).
- [34] J. Z. Sun and D. C. Ralph, *J. Magn. Magn. Mater.* **320**, 1227 (2008).
- [35] M. Julliere, *Phys. Lett. A* **54**, 225 (1975).
- [36] Y. Tserkovnyak, A. Brataas, G. E. W. Bauer, and B. I. Halperin, *Rev. Mod. Phys.* **77**, 1375 (2005).
- [37] N. Strelkov, A. Chavent, A. Timopheev, R. C. Sousa, I. L. Prejbeanu, L. D. Buda-Prejbeanu, and B. Dieny, *Phys. Rev. B* **98**, 214410 (2018).
- [38] G. Mihajlović, N. Smith, T. Santos, J. Li, M. Tran, M. Carey, B. D. Terris, and J. A. Katine, *Phys. Rev. Appl.* **13**, 024004 (2020).
- [39] J. Z. Sun, MMM B03-01 (2020).
- [40] M. Weisheit, S. Fähler, A. Marty, Y. Souche, C. Poinson, and D. Givord, *Science* **315**, 349 (2007).
- [41] T. Maruyama *et al.*, *Nature Nanotechnology* **4**, 158 (2009).
- [42] S. Miwa, K. Matsuda, K. Tanaka, Y. Kotani, M. Goto, T. Nakamura, and Y. Suzui, *Appl. Phys. Lett.* **107**, 162402 (2015).
- [43] C. Safranski and J. Z. Sun, *Phys. Rev. B* **100**, 014435 (2019).
- [44] D. C. Worledge, G. Hu, D. W. Abraham, J. Z. Sun, P. L. Trouilloud, J. Nowak, S. Brown, M. C. Gaidis, E. J. O'Sullivan, and R. P. Robertazzi, *Appl. Phys. Lett.* **98**, 022501 (2011).
- [45] S. Ikeda, K. Miura, H. Yamamoto, K. Mizunuma, H. D. Gan, M. Endo, S. Kanai, J. Hayakawa, F. Matsukura, and H. Ohno, *Nat. Mater.* **9**, 721 (2010).
- [46] M. Gajek *et al.*, *Appl. Phys. Lett.* **100**, 132408 (2012).
- [47] J. Z. Sun *et al.*, *Phys. Rev. B* **88**, 104426 (2013).
- [48] J. Z. Sun, SPIE Conference **9931**, 37 (2016).
- [49] J. J. Nowak *et al.*, *IEEE Magn. Lett.* **7**, 3102604 (2016).
- [50] G. Hu *et al.*, *IEEE Magn. Lett.* **10**, 4504304 (2019).
- [51] E. R. J. Edwards *et al.*, in *2020 IEEE International Electron Devices Meeting (IEDM)*, San Francisco (IEEE, 2020), p. 24.4.1.